In-situ 3D X-ray tomography under high-pressure H2: Direct observation and quantification of hydrogen-induced damage evolution in steel during tensile testing

L M Santana, Victor Okumko, A King, L Henry, C Bolitt, S Nicole, H Proudhon, T F Morgeneyer, Yazid Madi

International Journal of Hydrogen Energy 229 (2026) 154770

Contents lists available at ScienceDirect

International Journal of Hydrogen Energy

journal homepage: www.elsevier.com/locate/he

Short communication

In-situ 3D X-ray tomography under high-pressure H_2: Direct observation and quantification of hydrogen-induced damage evolution in steel during tensile testing

L.M. Santana [a], V. Okumko [a,b], A. King [b], L. Henry [b], C. Bolitt [c], S. Nicole [c], H. Proudhon [a], T.F. Morgeneyer [a], Y. Madi [a,*]

[a] Mines Paris - PSL, CMAT - Centre des Matériaux, CNRS UMR 7633, 21 Allée des Marronniers, Versailles, 78000, France
[b] Synchrotron SOLEIL, L'Orme des Merisiers, Départamentale 128, Saint-Aubin, 91190, France
[c] Top Industrie - High Pressure Technology, 79 Rue Hippolyte Marinoni, Vaux-le-Pénil, 77000, France

ARTICLE INFO

Keywords:
Hydrogen embrittlement
Three-dimensional tomography
Synchrotron radiation
Steels

ABSTRACT

We introduce a novel experimental device for tensile testing in high-pressure hydrogen environments, coupled with in situ 3D synchrotron X-ray tomography. Demonstrated on E355 steel, this setup enables repeated tomographic imaging during deformation, offering unprecedented time-resolved insight into hydrogen-assisted damage mechanisms. It allows full 3D quantification of crack and void volume, shape, orientation, and spatial distribution, opening new pathways for understanding hydrogen embrittlement at the microscale. Specimens were tested at 20 and 130 bar H_2 at a strain rate of 1×10^{-4} s^{-1}, with ductility loss of 20% at 20 bar and 69% at 130 bar. The new methodology enabled precise tracking of surface crack penetration during the test, which increased from 4 μm at the Ultimate Tensile Strength to an average of 24 μm near fracture at 130 bar. Finally, the approach enabled the direct observation of internal hydrogen-induced cracks coalescing with surface cracks, demonstrating their contribution to final fracture.

1. Introduction

The transition to a low-carbon energy system has increased interest in renewable hydrogen [1–4]. However, hydrogen is known to diffuse into metals and interacts with their microstructure, resulting in a possible degradation of mechanical properties. This phenomenon, known as hydrogen embrittlement (HE), has been studied for decades [5,6], and several mechanisms have been proposed [7–12], yet the governing processes remain debated [13]. A challenge in this debate is the limited ability to observe hydrogen-induced damage mechanisms within the bulk of specimens tested under hydrogen.

Three-dimensional (3D) X-ray tomography enables characterization of micrometer-scale damage, providing insight into void nucleation, growth, and coalescence [14,15]. Its application to hydrogen studies is expanding. Depraetere et al. [16,17] showed by ex-situ tomography that hydrogen accelerates fracture in X56 steel and alters void morphology in X70 steel. Konert et al. [18] reported hydrogen-induced changes in crack orientation in X65 pipeline steel. Maire et al. [19] showed by in-situ tomography that hydrogen pre-charging in austenitic stainless steels transforms spherical voids into micro-cracks perpendicular to the tensile axis. Our recent work [20] used ex-situ tomography to study E355 ferritic–pearlitic steel under 100 bar H_2, revealing brittle surface cracks and ductile bulk damage at moderate strain rates (5×10^{-4} s^{-1}), while low strain rates (1×10^{-5} s^{-1}), promoted deeper diffusion and internal embrittlement.

Previous tomography studies relied on post-mortem analysis or in-situ tests of pre-charged specimens, which is limiting for materials with high hydrogen diffusivity. In-situ mechanical testing during hydrogen exposure has so far been restricted to surface techniques, such as scanning electron microscopy [21,22]. Time-resolved X-ray tomography of hydrogen-induced damage during loading in a hydrogen environment has not yet been reported. Here, we address this gap by performing in-situ 3D X-ray tomography during tensile testing in pressurized hydrogen for the first time. An in-situ sample environment was developed to enable in-situ tomography scans during loading, capturing temporal evolution and allowing quantitative assessment of hydrogen-assisted damage, opening new opportunities to advance understanding of HE.

2. Methodology

A modified E355 steel tube was used in this study, with composition (at%) 0.15 C, 1.38 Mn, 0.19 Si, 0.04 Cr, 0.02 Ni, 0.01 Mo, 0.002 S,

* Corresponding author.
E-mail address: yazid.madi@minesparis.psl.eu (Y. Madi).

https://doi.org/10.1016/j.ijhydene.2026.154770
Received 24 February 2026; Received in revised form 20 March 2026; Accepted 26 March 2026
Available online 31 March 2026

and 0.015 P, balance Fe. Its microstructure consists of a ferritic matrix with elongated pearlite bands along Longitudinal (L) and Transverse (T) directions, average grain size 15.9 μm. SEM-EDS showed low inclusion content (0.06 vol%), mainly globular CaS and (Al, Mg) oxides, with average diameter of 0.25 μm. Further details are in [23].

Sub-size tensile specimens (mST-Φ_0 = 1.2 mm, L_0 = 2 mm, as shown in the detail of Fig. 1(a)) were machined along the L direction of the tube. Previous work by Madi et al. [24] showed that this geometry provides mechanical properties consistent with standard specimens. The same geometry was used in gaseous hydrogen tensile tests with interrupted loading and ex-situ 3D X-ray tomography for damage characterization [20].

Tensile tests were carried out at the SOLEIL synchrotron on the PSICHE beamline using a modified version of an in-situ tensile setup [25] incorporating a compact autoclave designed for high-pressure hydrogen exposure under X-ray irradiation. The principle of the experiment is depicted in Fig. 1(a). Prior to testing, the specimen is mounted in the autoclave, which is then connected to a gas panel. Ten purge cycles with nitrogen were followed by ten purge cycles with analytical-grade hydrogen to remove residual O_2 and H_2O, which are known to inhibit hydrogen embrittlement [26]. The autoclave was then filled with hydrogen to the desired test pressure, sealed, and transported to the beamline. Two hydrogen pressures were investigated for this initial study: 20 bar, representing moderate H_2 pressure, and 130 bar, corresponding to a higher charging condition.

An internal load cell measures the applied force directly on the specimen, eliminating the influence from sealing friction that affects external measurements, while load line displacement was controlled by the beamline control system, based on Tango.[1] Local deformation was monitored via radial strain measured from tomography data, following Madi et al. [24], because a mechanical extensometer could not be used in the confined volume. The radial strain is defined as the relative reduction in the minimum cross-sectional diameter measured along the tube short-transverse (thickness) direction ($\Delta\Phi_s/\Phi_0$), where Φ_0 is the initial diameter at the start of the test. The diameter is obtained by post-processing the radiographs to detect the specimen contour. Experiments were performed at a longitudinal strain rate of 1×10^{-4} s^{-1}, with loading periodically slowed down for tomography scans to capture damage evolution. Imaging was performed at a peak energy of 65 keV with an exposure time of 20 ms per projection. A total of 1500 projections were acquired, resulting in reconstructed datasets of 2048^3 voxels with a voxel size of 0.65 μm. This corresponds to an analyzed volume of ≈2.36 mm^3. Data processing and analysis was conducted using Thermo Scientific Avizo Software and the open source Python package Pymicro [27], similarly to our previous work [20].

3. Results

Fig. 1(b) shows the tensile response of sub-size specimens tested in gaseous hydrogen at 20 and 130 bar H_2 (blue and red curves, respectively). The black curve shows an air tensile test from our previous work [20], included as an inert reference and characterized by ex-situ tomography. Circles mark the loading steps where the displacement rate was reduced for X-ray tomography, enabling in-situ damage observation. Dotted lines show the evolution of total damage volume fraction, with squares indicating values from individual scans.

Three-dimensional renderings of segmented damage are shown for selected scans, illustrating its temporal and spatial evolution. Surface-connected damage appears in red, internal damage in green and blue, and the specimen geometry in semi-transparent gray. The damage classification is detailed later in Fig. 3, where the evolution of damage can also be more clearly observed.

[1] https://www.tango-controls.org/.

Stress–radial strain responses at both hydrogen pressures are similar up to the Ultimate Tensile Strength (UTS), indicating little effect of hydrogen on initial plastic deformation, but clear differences appear beyond the UTS. The specimen tested at 20 bar H_2 reaches a higher radial strain at failure ($\Delta\Phi_s/\Phi_0$ = 0.446, corresponding to an area reduction of 69.3%), compared to the specimen tested at 130 bar H_2 ($\Delta\Phi_s/\Phi_0$ = 0.172, area reduction 31.4%). The area reduction is calculated assuming a circular cross-section, using $R.A. = 1 - (1 - \Delta\Phi_s/\Phi_0)^2$. For reference, typical air tests from our previous work yield $\Delta\Phi_s/\Phi_0$ = 0.56 (area reduction 80.6%) [20,24].

Based on these values, the corresponding hydrogen embrittlement indices (HEI), defined as

$$\mathrm{HEI} = \left(1 - \frac{(\Delta\Phi_s/\Phi_0)_{H_2}}{(\Delta\Phi_s/\Phi_0)_{air}}\right) \times 100 \quad (1)$$

which yield approximately 20.4% at 20 bar and 69.3% at 130 bar.

The evolution of damage volume fraction accentuates the difference in behavior. The damage volume fraction is calculated as the ratio of the total volume of damage captured in the tomography scan to the scanned specimen volume at each loading step, which changes as the specimen deforms. At 20 bar H_2, the damage volume fraction increases gradually, followed by a marked acceleration near failure (around $\Delta\Phi_s/\Phi_0 \approx 0.3$). The total damage volume fraction measured in the last scan prior to rupture is 5.87×10^{-3}. In contrast, at 130 bar H_2, damage initiates earlier and grows much more rapidly immediately after the UTS, at approximately $\Delta\Phi_s/\Phi_0 \approx 0.1$. The total damage volume fraction in the final scan before rupture reaches 1.40×10^{-2}, which is approximately 2.4 times higher than in the 20 bar condition. For reference, the air test exhibits a final damage volume fraction of 4.38×10^{-3}, remaining below the values measured under hydrogen.

Analysis of the three-dimensional visualizations reveals pronounced differences in damage distribution. At 20 bar H_2, damage develops predominantly in the central region of the specimen (blue), with limited surface damage (red). In contrast, at 130 bar H_2, surface damage becomes increasingly dominant as deformation progresses.

As the tests differed primarily in extent and progression of surface damage, a methodology was developed to quantify hydrogen-induced surface crack penetration from 3D X-ray tomography data.

The methodology was applied here to the tensile test conducted under 130 bar H_2, as depicted in Fig. 2(a). The 50 largest surface cracks were selected based on their volume. For each selected crack, the radial distance of each voxel was calculated with respect to the specimen center. In the next step, the deepest 5% of crack voxels (depicted in black in Fig. 2(a)), were retained. The penetration depth of an individual crack was then defined as the average radial distance of these deepest 5% of voxels. The accompanying probability density plot (Fig. 2(a), right) illustrates the distribution of voxel penetration depths for a representative crack, with the black region highlighting the voxels used to calculate the average penetration, further clarifying the methodology. This approach was selected because it provides a robust and reproducible measure of crack penetration, focusing on the deepest regions while minimizing the influence of surface irregularities and reconstruction artifacts.

Fig. 2(b) presents the engineering stress (F/S_0) - radial strain ($\Delta\Phi_s/\Phi_0$) response for the specimen tested at 130 bar H_2, together with boxplots summarizing the penetration depth of the 50 largest hydrogen-induced surface cracks. The boxplots correspond to successive tomographic scans acquired from the UTS up to the final scan prior to fracture. The box represents the central 50% of the data, with the orange line indicating the median value. The whiskers extend to 1.5 times this central range, and any points beyond them are plotted individually as outliers (white circles).

The figure clearly quantifies the evolution of surface crack penetration during the tensile test. The first two boxplots, corresponding to the UTS and just before UTS, show average penetration depths of ≈4.3 μm, with a few outliers in the second boxplot reaching up to 15.9 μm,

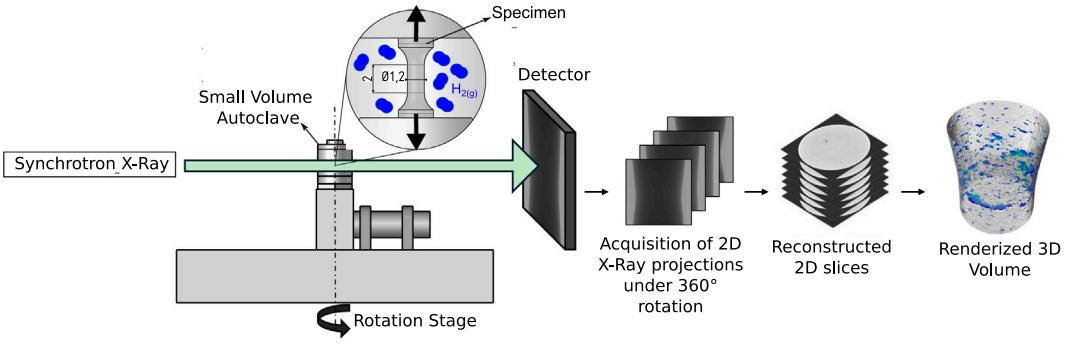

(a) Experimental setup for in-situ tensile testing under high-pressure hydrogen during synchrotron X-ray tomography.

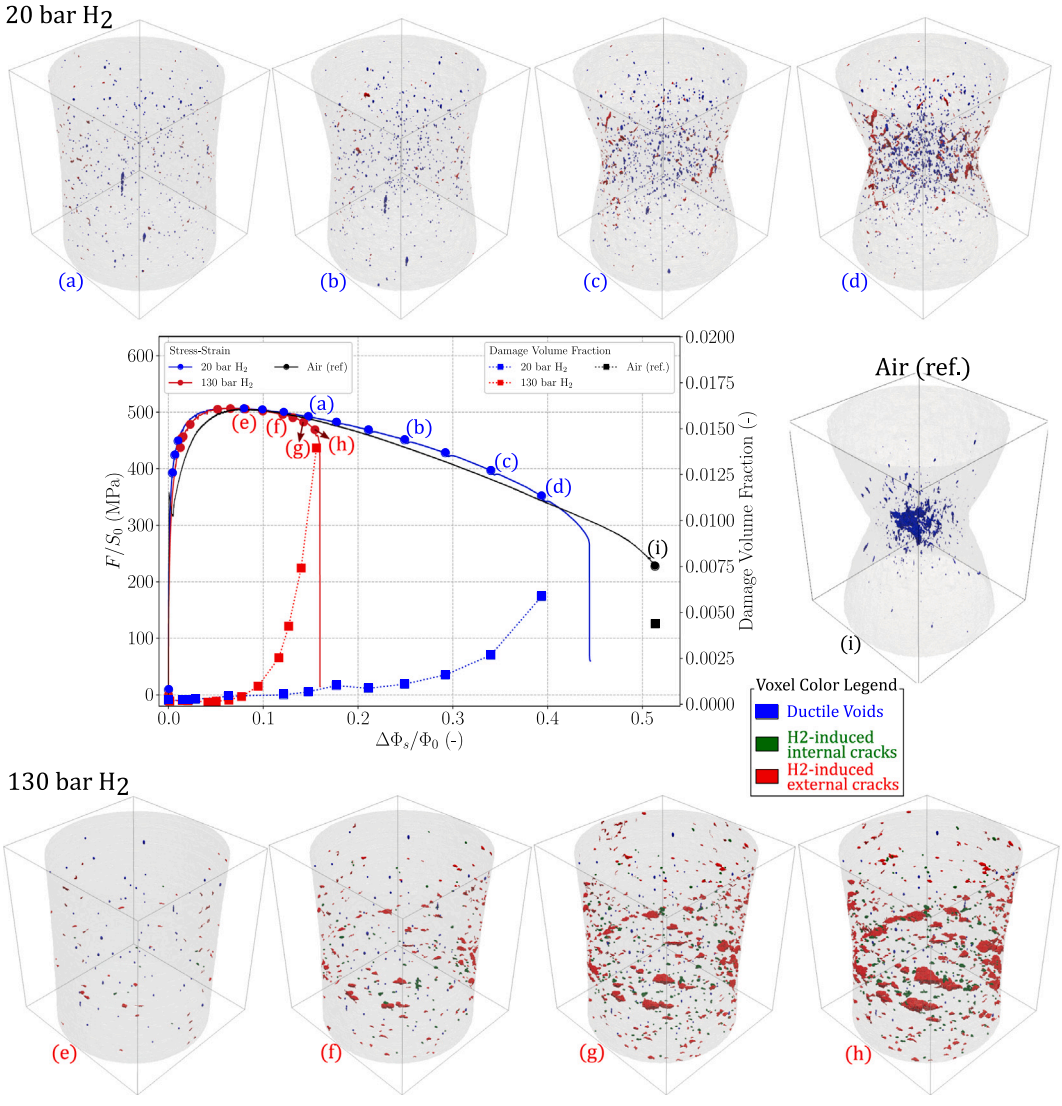

(b) Tensile behavior and damage evolution at 20 and 130 bar H_2.

Fig. 1. Fig. 1(a) shows a schematic view of the in-situ tensile testing setup developed for high-pressure hydrogen experiments, featuring a compact autoclave compatible with synchrotron X-ray tomography. Fig. 1(b) presents engineering stress (F/S_0) - radial strain ($\Delta\Phi_s/\Phi_0$) curves for sub-size specimens tested at 20 and 130 bar H_2, highlighting tomography acquisition steps (circles), and total damage volume evolution (squares). Selected 3D renderings illustrate the spatial and temporal progression of internal and external damage, which classification is detailed later in Fig. 3.

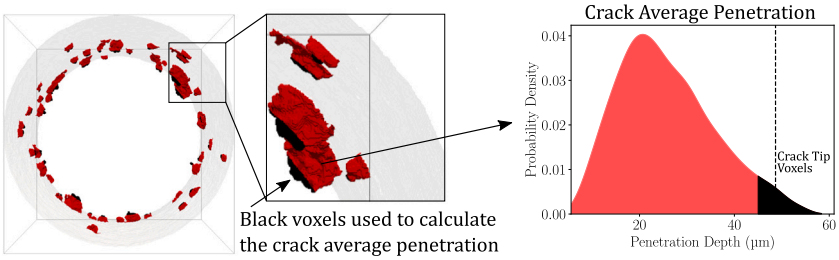

(a) Methodology for quantifying hydrogen-induced surface crack penetration.

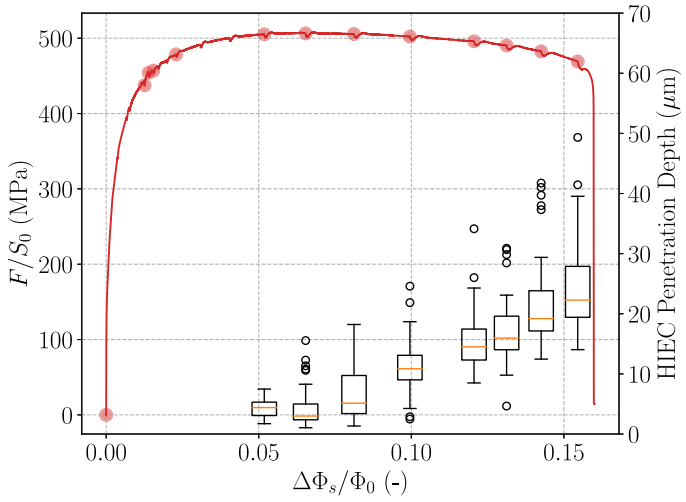

(b) Evolution of crack penetration depth during the 130 bar H_2 tensile test.

Fig. 2. (2(a)) Illustration of the methodology used to quantify hydrogen-induced surface crack penetration from 3D X-ray tomography. For each of the 50 largest cracks, the penetration depth was defined as the average distance to the specimen center of the deepest 5% of their voxels. (2(b)) Engineering stress–radial strain response for the 130 bar H_2 test with boxplots showing the evolution of crack penetration depth across successive scans from UTS to fracture. Crack penetration starts at UTS, increasing from 4.3 μm to an average of ≈24.4 μm.

indicating a small fraction of deeper cracks. In subsequent steps, penetration progressively increases and becomes more heterogeneous, as indicated by the appearance of multiple outliers, with averages rising from ≈7.0 μm (third boxplot) to ≈21.4 μm (second-to-last boxplot). The final scan exhibits the most advanced damage, ranging from 14 to 49 μm, with an average of ≈24.4 μm, revealing the presence of deeply penetrating cracks.

Building on the surface crack penetration analysis, the morphology and orientation of all damage features are examined to understand the contributions of internal and external cracks and the differences between the 20 bar and 130 bar tests.

The morphology and orientation of each damage feature were quantified using an approach adapted from Denis et al. [28], based on a shape factor and alignment of major axis relative to the loading axis (γ angle). For further details, the reader is referred to Denis et al. [28] and Santana et al. [20]. This procedure enabled the separation of damage into three distinct groups, illustrated by the three-dimensional visualizations in Fig. 3(a).

Damage features were classified according to quantitative criteria derived from 3D X-ray tomography data. Surface cracks (red) were defined as damage features having at least one voxel in contact with the specimen's exterior envelope, corresponding to Hydrogen-Induced External Cracks (HIEC). As illustrated in Fig. 3(a), these cracks nucleate and coalesce with an ellipsoidal morphology, their major axes oriented perpendicular to the loading axis, progressively penetrating into the specimen.

Group 1 (blue) comprises internal damage features exhibiting near-spherical morphology (shape factor > 0.8) or elongation primarily aligned with the loading axis ($\gamma < 30°$), corresponding to ductile voids formed by nucleation and growth within the bulk material. These features typically nucleate around inclusions as spherical cavities and coalesce into prolate ellipsoids with their major axis parallel to the loading direction, commonly referred to as "necktie" morphology [14] (Fig. 3(a)).

Group 2 (green) consists of internal damage features whose major axes are oriented approximately perpendicular to the loading axis ($\gamma > 60°$), indicative of Hydrogen-Induced Internal Cracks (HIIC), consistent with previous observations by Santana et al. [20]. These features generally nucleate as slightly oblate ellipsoids and evolve into flat, elongated ellipsoids (Fig. 3(a)).

Three-dimensional renderings of specimens tested under 20 bar and 130 bar H_2 are shown in Figs. 3(b) and 3(c). Seven 45° circular sectors, arranged in a circular layout, represent successive loading steps at the same position within the specimen, illustrating local damage evolution in a fixed region. A surrounding circular scale indicates radial strain ($\Delta\Phi/\Phi_0$). Damage features are color-coded as previously described: blue for ductile voids, red for HIEC, and green for HIIC.

In the 20 bar H_2 test, damage evolves progressively, with ductile voids nucleating and coalescing into elongated prolate ellipsoids. Surface cracks appear only at late stages, forming a sparse peripheral network, while the interior remains predominantly governed by ductile void growth.

Under 130 bar H_2, HIEC nucleate immediately after UTS, propagating rapidly from the periphery and coalescing earlier than at 20 bar. Ductile void growth is limited, while HIIC nucleate preferentially in

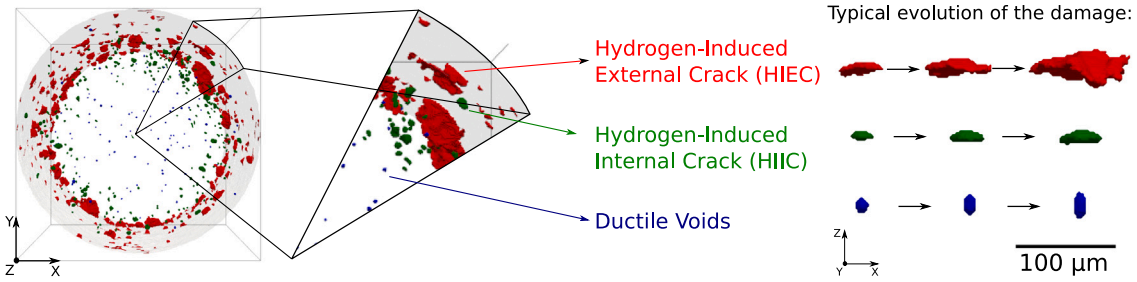

(a) Quantitative classification of damage based on morphology and orientation criteria.

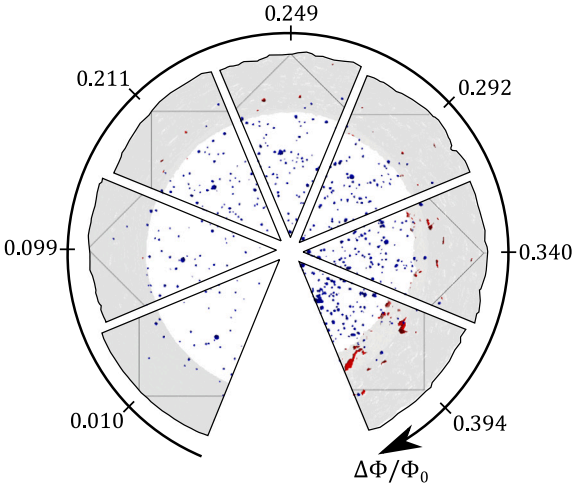

(b) 3D damage evolution during tensile test under 20 bar H_2

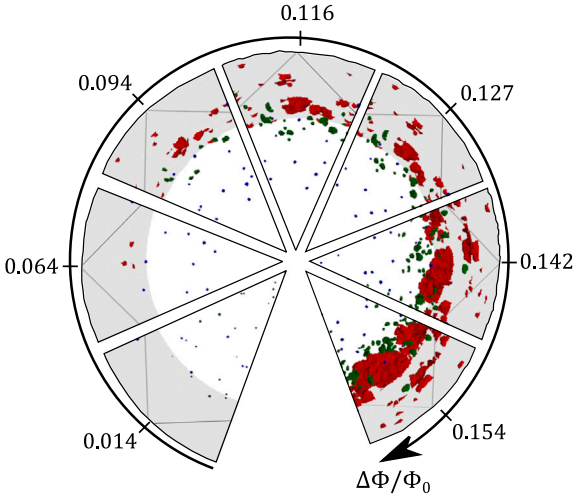

(c) 3D damage evolution during tensile test under 130 bar H_2.

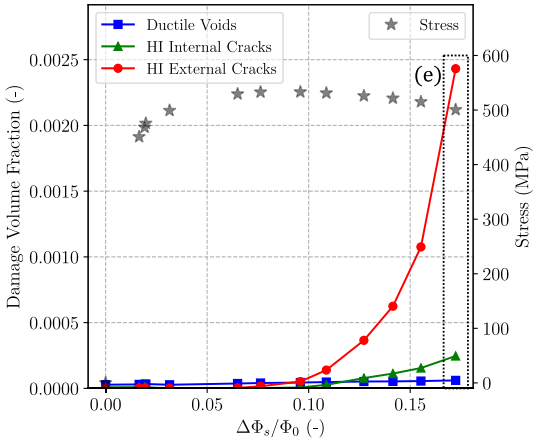

(d) Evolution of damage volume fraction at 130 bar H_2.

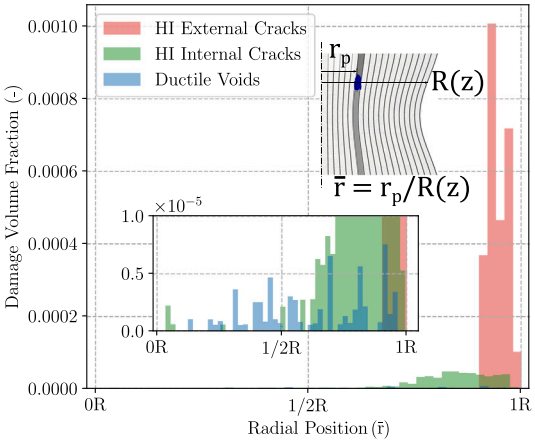

(e) Radial distribution of damage volume fraction before rupture (130 bar H_2).

Fig. 3. Three-dimensional characterization and quantitative analysis of damage during tensile tests in hydrogen. (3(a)) Schematic representation of the classification procedure based on shape factor and orientation relative to the loading axis, distinguishing Ductile Voids (blue), Hydrogen-Induced External Cracks (HIEC, red), and Hydrogen-Induced Internal Cracks (HIIC, green). (3(b)–3(c)) 3D renderings of the same location at successive loading steps for tests performed under 20 bar and 130 bar H_2, respectively, with radial strain indicated. (3(d)) Evolution of the damage volume fraction for each mechanism at 130 bar H_2. (3(e)) Radial distribution of damage volume fraction in the last scan prior to rupture at 130 bar H_2. The images highlight the progressive, void-dominated damage at 20 bar, in contrast with the rapid surface crack penetration and HIIC formation at 130 bar. (For interpretation of the references to color in this figure legend, the reader is referred to the web version of this article.)

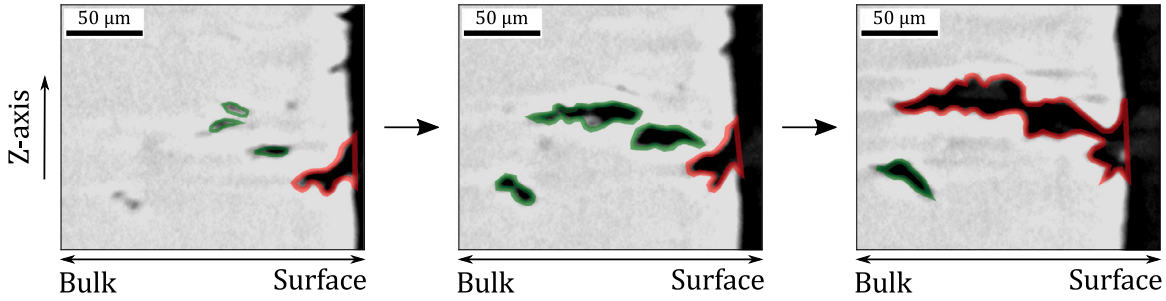

(a) 2D slices showing the coalescence of Hydrogen-Induced Internal Cracks (HIIC, green) with Hydrogen-Induced External Cracks (HIEC, red) during tensile loading at 130 bar H_2.

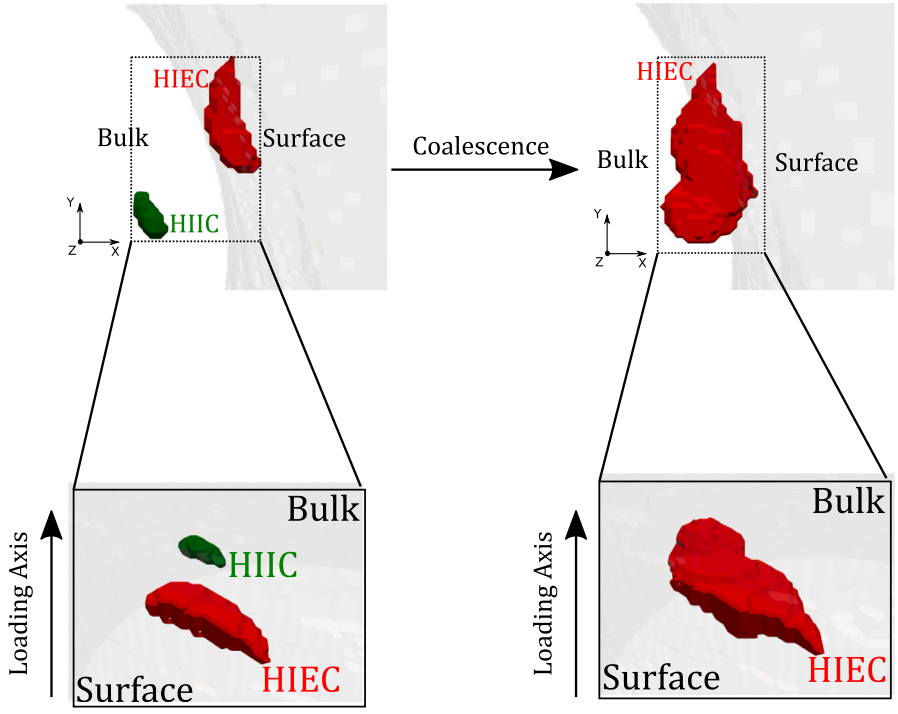

(b) 3D depiction of a coalescence event involving Hydrogen-Induced Internal Cracks (HIIC, green) and Hydrogen-Induced External Cracks (HIEC, red) during the 130 bar H_2 tensile test.

Fig. 4. Coalescence of hydrogen-induced cracks during tensile loading under 130 bar H_2, shown in 2D slices at 4(a) and in 3D at 4(b). Red indicates Hydrogen-Induced External Cracks (HIEC), while green shows Hydrogen-Induced Internal Cracks (HIIC). Initially, HIEC and HIIC are distinct, but during deformation they progressively coalesce, forming continuous cracks that link the interior to the surface. Despite their smaller volume fraction, HIIC play an important role, accelerating crack propagation and ultimately leading to hydrogen-assisted failure. (For interpretation of the references to color in this figure legend, the reader is referred to the web version of this article.)

the sub-surface region and rarely near the center, reflecting limited hydrogen diffusion. These HIIC, though less volumetrically dominant than surface cracks, are a clear signature of hydrogen-assisted damage, and will be addressed in greater detail later in this work.

Fig. 3(d) shows the evolution of damage volume fractions under 130 bar H_2, defined as the volume of a given mechanism divided by the specimen volume at each stage. Beyond UTS, HIEC dominate damage volume growth, with HIIC increasing in the last scans and ductile voids contributing negligibly.

Fig. 3(e) quantifies the radial damage distribution in the last scan prior to rupture for the tensile test conducted under 130 bar H_2. Each feature was segmented and its barycenter determined. Radial position in the deformed geometry is normalized as:

$$\bar{r} = \frac{r_p}{R(z)} \tag{2}$$

where r_p is the distance from the specimen centerline and $R(z)$ the local radius at the barycenter height. Here, $\bar{r} = 0$ (0R) corresponds to the center and $\bar{r} = 1$ (1R) to the surface.

The specimen's deformed volume is divided into concentric radial intervals, which serve as histogram bins. Each detected damage feature is assigned to a bin according to its normalized radial position, $\bar{r}$, for volume analysis, as illustrated in Fig. 3(e).

The results indicate that, at this stage of the test, HIEC are confined to ≈10% of the radius near the surface. In contrast, HIIC are

predominantly located in the sub-surface region and extend toward the mid-radius. Ductile voids are distributed across the entire radius, consistent with their association with pre-existing globular inclusions.

4. Discussion

Although HIIC represent a relatively small fraction of the total damage volume at 130 bar H_2, their spatial localization and morphology suggest a significant role in the fracture process. HIIC preferentially form in the sub-surface region with major axis perpendicular to the loading direction, making them mechanically compatible with the advancing HIEC. This complementarity raises the question of whether HIIC are merely secondary features or actively contribute to crack propagation through interaction and coalescence with surface cracks.

Fig. 4(a) presents 2D tomography slices illustrating the coalescence of HIIC (green) with HIEC (red) during the final three stages of the 130 bar H_2 tensile test. Initially, four distinct cracks are visible: three HIIC and one HIEC. In subsequent scans, HIIC grow while the HIEC progressively connects with them, forming a continuous crack path from the surface into the bulk. Despite their smaller volume fraction, HIIC act as precursors that facilitate crack linkage and propagation.

Fig. 4(b) provides a 3D view of another coalescence event. The upper panels show the relative positions of the HIIC in the sub-surface region and the HIEC at the surface prior to coalescence. The lower panels present a zoomed 3D view along the loading axis, highlighting how HIEC progressively links with the nearby HIIC, forming a continuous crack path extending into the bulk.

As HIIC develop preferentially in the sub-surface region and extend deeper than HIEC (Fig. 3(e)), their coalescence with surface cracks suggests an active role in HIEC propagation. This interaction may explain the outliers observed in the final steps of Fig. 2(b), where unusually deep surface cracks appear. Moreover, the coalescence process implies a partial "volume transfer" from HIIC to HIEC, consistent with the evolution of damage volume fractions depicted in Fig. 3(d). Altogether, these observations support the conclusion that HIIC act not only as indicators of sub-surface hydrogen-assisted damage but also as facilitators of surface crack propagation, contributing to the final fracture process under high-pressure hydrogen environment.

5. Conclusions

The present work demonstrates, for the first time, the use of in-situ 3D X-ray tomography to monitor hydrogen-assisted damage evolution in steel during tensile loading under high-pressure hydrogen gas. The developed setup enabled repeated scans throughout tensile testing, providing time-resolved, three-dimensional insight into damage nucleation, growth and coalescence at 20 bar and 130 bar H_2. While similar mechanical responses were observed up to the Ultimate Tensile Strength (UTS), distinct damage mechanisms emerged beyond this point depending on hydrogen pressure. Quantitative 3D analysis revealed a transition from predominantly ductile void growth at 20 bar H_2 to damage dominated by Hydrogen-Induced External Cracks (HIEC) at 130 bar H_2. The specimen tested at 20 bar H_2 reached a radial strain at failure of $\Delta\Phi_s/\Phi_0 = 0.446$ (69.3% area reduction), whereas at 130 bar H_2 failure occurred earlier at $\Delta\Phi_s/\Phi_0 = 0.172$ (31.4% area reduction). This ductility loss was accompanied by a marked increase in total damage volume fraction prior to rupture, reaching 1.40 % at 130 bar compared to 0.59 % at 20 bar.

At 20 bar H_2, damage was dominated by ductile void nucleation and coalescence in the specimen core, with limited surface cracking. In contrast, at 130 bar H_2, HIEC became the main contributor to damage growth beyond the UTS, with penetration depths increasing from ≈4.3 μm near UTS to ≈24.4 μm in the final scan, reaching maximum values of 49 μm. Hydrogen-Induced Internal Cracks (HIIC) were mainly localized in the sub-surface region (up to 1/2R) and interacted with HIEC. Their progressive coalescence indicates that HIIC facilitate HIEC advance, contributing to crack linkage and final fracture despite their smaller volume fraction.

The proposed methodology enables quantitative classification of voids, HIIC, and HIEC based on morphology and spatial distribution, as well as direct tracking of crack penetration depth in 3D. By combining in-situ imaging with quantitative damage analysis, this work provides new insight into hydrogen embrittlement mechanisms and establishes a robust experimental platform for predictive modeling and the design of hydrogen-resistant materials.

CRediT authorship contribution statement

L.M. Santana: Writing – review & editing, Writing – original draft, Visualization, Validation, Software, Resources, Methodology, Investigation, Formal analysis, Data curation, Conceptualization. **V. Okumko:** Writing – review & editing, Visualization, Validation, Resources, Methodology, Investigation, Formal analysis, Data curation. **A. King:** Writing – review & editing, Validation, Supervision, Software, Resources, Project administration, Methodology, Investigation, Funding acquisition, Formal analysis, Data curation, Conceptualization. **L. Henry:** Writing – review & editing, Validation, Resources, Investigation, Formal analysis, Data curation. **C. Bolitt:** Validation, Resources, Methodology, Conceptualization. **S. Nicole:** Validation, Resources, Methodology, Conceptualization. **H. Proudhon:** Writing – review & editing, Visualization, Validation, Supervision, Software, Project administration, Methodology, Investigation, Funding acquisition, Data curation, Conceptualization. **T.F. Morgeneyer:** Writing – review & editing, Writing – original draft, Visualization, Validation, Supervision, Resources, Project administration, Methodology, Investigation, Funding acquisition, Formal analysis, Data curation, Conceptualization. **Y. Madi:** Writing – review & editing, Writing – original draft, Visualization, Validation, Supervision, Resources, Project administration, Methodology, Investigation, Funding acquisition, Formal analysis, Data curation, Conceptualization.

Declaration of competing interest

The authors declare that they have no known competing financial interests or personal relationships that could have appeared to influence the work reported in this paper.

Acknowledgments

This work was conducted during SOLEIL beamtime 20241968, with partial support from the HyWay project (Grant Agreement No. 101135374) and ANR Chair Program MESSIAH (ANR-20-CHIN-0003). It has also received partial support under the Seed Program of PSL Research University "MATRIX" launched by PSL Research University and implemented by ANR with the references ANR-10-IDEX-0001. The authors gratefully acknowledge the SESAMES technical staff (Youssef Atik, Maryse Gille, and Yann Auriac) and the workshop (Frédéric Coutard) at the Centre des Matériaux, Mines Paris — PSL, as well as the SOLEIL Safety team (Jean-Pierre Laurent, Laurent Germain, Danielle Njinwoua, Sara Traat) and the SOLEIL Materials Laboratory (Mathieu Chevrot and Stefan Kubsky) for their valuable technical support.

References

[1] Haeseldonckx D, D'haeseleer W. The use of the natural-gas pipeline infrastructure for hydrogen transport in a changing market structure. Int J Hydrog Energy 2007;32(10):1381–6. http://dx.doi.org/10.1016/j.ijhydene.2006.10.018.

[2] Laureys A, Depraetere R, Cauwels M, Depover T, Hertelé S, Verbeken K. Use of existing steel pipeline infrastructure for gaseous hydrogen storage and transport: A review of factors affecting hydrogen induced degradation. J Nat Gas Sci Eng 2022;101:104534. http://dx.doi.org/10.1016/j.jngse.2022.104534.

[3] Zhang C, Shao Y, Shen W, Li H, Nan Z, Dong M, Bian J, Cao X. Key technologies of pure hydrogen and hydrogen-mixed natural gas pipeline transportation. ACS Omega 2023;8(22):19212–22. http://dx.doi.org/10.1021/acsomega.3c01131.

[4] Cerniauskas S, Jose Chavez Junco A, Grube T, Robinius M, Stolten D. Options of natural gas pipeline reassignment for hydrogen: Cost assessment for a Germany case study. Int J Hydrog Energy 2020;45(21):12095–107. http://dx.doi.org/10.1016/j.ijhydene.2020.02.121.
[5] Johnson W. On some remarkable changes produced in iron and steel by the action of hydrogen and acids. Proc R Soc Lond 1875;23(156):168–79. http://dx.doi.org/10.1098/rspl.1874.0024.
[6] Hirth J. Effects of hydrogen on the properties of iron and steel. AIME 1980;11A:861–90. http://dx.doi.org/10.1007/BF02654700.
[7] Ferreira P, Robertson I, Birnbaum H. Hydrogen effects on the character of dislocations in high-purity aluminium. Acta Mater 1999;47:2991–8. http://dx.doi.org/10.1016/S1359-6454(99)00156-1.
[8] Beachem CD. A new model for hydrogen-assisted cracking (hydrogen "embrittlement"). Met Trans 1972;3(2):441–55. http://dx.doi.org/10.1007/BF02642048.
[9] Barnoush A, Vehoff H. Recent developments in the study of hydrogen embrittlement: hydrogen effect on dislocation nucleation. Acta Mater 2010;58:5274–85. http://dx.doi.org/10.1016/j.actamat.2010.05.057.
[10] Troiano AR. The role of hydrogen and other interstitials in the mechanical behavior of metals: (1959 Edward De Mille Campbell Memorial Lecture). Met Microstruct Anal 2016;5(6):557–69. http://dx.doi.org/10.1007/s13632-016-0319-4.
[11] Lynch S. Hydrogen embrittlement phenomena and mechanisms. Corros Rev 2012;30(3). http://dx.doi.org/10.1515/corrrev-2012-0502.
[12] Nagumo M, Nakamura M, Taka K. Hydrogen thermal desorption relevant to delayed-fracture susceptibility of high-strength steels. Met Mater Trans A 2001;32:339–47. http://dx.doi.org/10.1007/s11661-001-0265-9.
[13] Djukic MB, Bakic GM, Sijacki Zeravcic V, Sedmak A, Rajicic B. The synergistic action and interplay of hydrogen embrittlement mechanisms in steels and iron: Localized plasticity and decohesion. Eng Fract Mech 2019;216:106528. http://dx.doi.org/10.1016/j.engfracmech.2019.106528.
[14] Madi Y, Garcia J-M, Proudhon H, Shinohara Y, Helfen L, Besson J, Morgeneyer TF. On the origin of the anisotropic damage of X100 line pipe steel: Part I—In situ synchrotron tomography experiments. Integr Mater Manuf Innov 2019;8(4):570–96. http://dx.doi.org/10.1007/s40192-019-00165-0.
[15] Morgeneyer TF, Starink MJ, Sinclair I. Evolution of voids during ductile crack propagation in an aluminium alloy sheet toughness test studied by synchrotron radiation computed tomography. Acta Mater 2008;56(8):1671–9. http://dx.doi.org/10.1016/j.actamat.2007.12.019.
[16] Depraetere R, De Waele W, Cauwels M, Depover T, Verbeken K, Boone M, Hertelé S. Influence of stress triaxiality on hydrogen assisted ductile damage in an X70 pipeline steel. Mater Sci Eng: A 2023;864:144549. http://dx.doi.org/10.1016/j.msea.2022.144549.
[17] Depraetere R, De Waele W, Cauwels M, Depover T, Verbeken K, Hertelé S. Damage evolution of a hydrogen charged grade X56 pipeline steel evaluated using X-ray micro-CT. Procedia Struct Integr 2024;54:172–9. http://dx.doi.org/10.1016/j.prostr.2024.01.070.
[18] Konert F, Wieder F, Nietzke J, Meinel D, Böllinghaus T, Sobol O. Evaluation of the impact of gaseous hydrogen on pipeline steels utilizing hollow specimen technique and μCT. Int J Hydrog Energy 2024;59:874–9. http://dx.doi.org/10.1016/j.ijhydene.2024.02.005.
[19] Maire E, Grabon S, Adrien J, Lorenzino P, Asanuma Y, Takakuwa O, Matsunaga H. Role of hydrogen-charging on nucleation and growth of ductile damage in austenitic stainless steels. Mater 2019;12(9):1426. http://dx.doi.org/10.3390/ma12091426.
[20] Santana LM, Okumko V, King A, Morgeneyer TF, Besson J, Madi Y. Investigating the influence of strain rate on hydrogen embrittlement in steel sub-size tensile specimens using 3D X-ray tomography. Int J Hydrog Energy 2025;138:626–47. http://dx.doi.org/10.1016/j.ijhydene.2025.04.398.
[21] Kim J, Tasan CC. Microstructural and micro-mechanical characterization during hydrogen charging: An in-situ scanning electron microscopy study. Int J Hydrog Energy 2019;44(12):6333–43. http://dx.doi.org/10.1016/j.ijhydene.2018.10.128.
[22] Koyama M, Yang Z, Xu W, Akiyama E. Localized plasticity, transformation, and martensite cracking in hydrogen-charged metastable austenitic stainless steel studied by in situ electron channeling contrast imaging. Mater Charact 2026;233:116127. http://dx.doi.org/10.1016/j.matchar.2026.116127.
[23] Santana L, Pinto DL, Osipov N, Furtado J, Bourguignon F, Marchais P-J, Madi Y, Besson J. Study of hydrogen embrittlement in steels using modified pressurized disks. Int J Hydrog Energy 2024-10;88:498–514. http://dx.doi.org/10.1016/j.ijhydene.2024.09.165.
[24] Madi Y, Santana L, Belkacemi S, Farrugia V, Meddour A, Marchais P-J, Bertin M, Furtado J. Mechanical characterization of hydrogen embrittlement in a gaseous environment: An innovative test setup using sub-size specimens. Eng Fail Anal 2024;162:108362. http://dx.doi.org/10.1016/j.engfailanal.2024.108362.
[25] Pelerin M, King A, Laiarinandrasana L, Proudhon H. Development of a versatile mechanical testing device for in situ synchrotron tomography and diffraction experiments. Integr Mater Manuf Innov 2019;8(3):378–87. http://dx.doi.org/10.1007/s40192-019-00143-6.
[26] Fernández-Pisón P, Santana LM, Sellam Q, Farrugia V, Madi Y, Besson J. Oxygen-mediated inhibition of gaseous hydrogen embrittlement in pipeline steels: Sub-size specimen testing and coupled diffusion-damage modeling. Int J Solids Struct 2026;113832. http://dx.doi.org/10.1016/j.ijsolstr.2026.113832.
[27] Marano A, Ribart C, Proudhon H. Towards a data platform for multimodal 4D mechanics of material microstructures. Mater Des 2024;246:113306. http://dx.doi.org/10.1016/j.matdes.2024.113306.
[28] Denis EP, Barat C, Jeulin D, Ducottet C. 3D complex shape characterization by statistical analysis: Application to aluminium alloys. Mater Charact 2008;59(3):338–43. http://dx.doi.org/10.1016/j.matchar.2007.01.012.